Journal of Advanced Ceramics
2024, **13**(12): 1965–1973
https://doi.org/10.26599/JAC.2024.9220989

Research Article

Stabilizing oxygen vacancies and promoting electrostrain in lead-free potassium niobate-based piezoelectrics over wide temperature ranges

Bingcheng Luo[1], Wei Feng[2], Suwei Dai[3], Hongzhou Song[4], Yunyi Wu[5], Jie Zhang[6]✉

[1] *College of Science, China Agricultural University, Beijing 100083, China*
[2] *State Key Laboratory of New Ceramics and Fine Processing, School of Materials Science and Engineering, Tsinghua University, Beijing 100084, China*
[3] *School of Materials Science and Technology, China University of Geosciences Beijing, Beijing 100083, China*
[4] *Institute of Applied Physics and Computational Mathematics, Beijing 100094, China*
[5] *Research Center for Comprehensive Energy Technology, CTG Science and Technology Research Institute, Beijing 100038, China*
[6] *Research Center for Metamaterials, Wuzhen Laboratory, Jiaxing 314500, China*

Received: August 18, 2024; Revised: September 27, 2024; Accepted: October 16, 2024

Abstract: Piezoelectric ceramics provide high strain and large driving forces in actuators. A large electrostrain can be realized by the introduction of point defects such as vacancies, interstitial defects, and substitution defects. With Mn doping, a significant increase in the reversible electrostrain from 0.05% to 0.17% could be achieved in potassium niobite lead-free piezoelectric ceramics. The origins of the large electrostrain were analyzed via *in situ* X-ray diffraction (XRD) under an electric field. The electrostrain and other typical electrical properties of the samples were measured at various temperatures, which enabled the ceramics to perform under a very wide temperature range, such as −80–130 °C for the 0.5 mol% Mn-doped sample with low dielectric loss (≤ 0.02). More importantly, combined with characterizations of the defect behavior by thermally stimulated depolarization current (TSDC), the failure mechanisms of electrostrain in a high-temperature environment could be revealed, which was associated with synergistic damage to the defects caused by the electric field and high temperature. The results can provide good ideas and a basis for the design of piezoelectric materials with good electrostrain stability over a wide temperature range.

Keywords: piezoelectric ceramic; lead-free; point defect; electrostrain; thermally stimulated depolarization current (TSDC)

1 Introduction

Environmentally friendly alkali niobium-based lead-free piezoelectric materials have immense potential for replacing lead-containing piezoelectric materials [1–6], especially for applications involving mechanical-to-electrical energy conversion, such as piezoelectric actuators [7–11]. The magnitude of electrostrain and temperature stability are the two most crucial parameters of piezoelectric actuators. Numerous studies have reported a narrow electrostrain gap between lead-free ceramics and lead-based ceramics [12–18]. However, there is still great interest in improving the temperature stability of electrostrain for ceramics operated over a wide temperature range to meet the requirements of harsh environments [19]. For alkali niobium-based piezoelectric ceramics, a general approach for improving the temperature stability of electrostrain is considered the diffusion phase transition, which arises from doping with multiple ions [20–22]. Additionally, a greater piezoelectric response can be obtained due to the presence of polycrystalline phase transitions (PPTs) [23]. However, the compositions of these lead-free ceramics with PPTs are usually very complex and difficult to reproduce [24]. Therefore, the influence of defects on the temperature stability of electrostrain remains a great challenge that urgently needs to be discussed [25,26].

Among various heterogeneous ion doping methods, manganese (Mn) ions are usually chosen as effective dopants for ABO_3 perovskite piezoelectric ceramics with A/B site substitutions because of their multiple valences and the role of sintering additives [14,27–31]. For example, by introducing Mn, a double hysteresis loop and a large recoverable electrostrain were achieved in tetragonal $(K,Li)(Nb,Ta)O_3$-based ceramics, and the electrostrain continued to decrease with increasing temperature [27]. Similar double hysteresis loops have also been reported in several other studies, and an aging process is generally required [28,31,32]. Kim *et al.* [29] achieved a double hysteresis loop and high electrical strain by controlling the sintering process without an aging process. However, an internal electric field formed after the polling process, suggesting the presence of defects in the unstable state. Although it is generally understood that ceramics can maintain a high strain of 0.2% at 200 °C, the motion of the defects in the hysteresis loops might not be able to keep up with the 5 Hz perturbation during electric field testing, making accurate measurement of the electrical strain profile at such high temperatures difficult. It has been suggested that point defects play an important role in electrostrain and related properties [33–38]. Defect dipoles, with the interactions of oxygen vacancies and

✉ Corresponding author.
E-mail: zjie_mse@163.com

manganese ions at niobium sites, can provide a driving force to switch the aligned domains back to their initial randomly distributed state [39–41]. Therefore, it is crucial to understand the behavior of defect dipoles to explore the good electrostrain performance of lead-free piezoelectric ceramics over a wide temperature range.

Recently, the thermally stimulated depolarization current (TSDC) technique has served as a powerful tool to identify the types of defects and gain insight into the behaviors of the defects that may exist in materials, especially oxygen vacancy-related point defects [42–44]. In this work, single-ion doping of Mn was introduced into typical $KNbO_3$ ceramics, and the electrostrain improved effectively. Combined with the characterization of the TSDC and electric properties, the effects of point defects on the temperature stability of the electrostrain in the Mn-doped $KNbO_3$ ceramics were also investigated.

2 Experimental

The piezoelectric ceramic $K(Mn_xNb_{1-x})O_3$ (abbreviated as KMN-x; x = 0, KMN-0; x = 0.5%, KMN-0.5; x = 1.0%, KMN-1.0; x = 1.5%, KMN-1.5) was prepared via a conventional solid-state reaction method. The corresponding oxides or carbonates, namely, K_2CO_3 (99.0% purity), Nb_2O_5 (99.5% purity), and $MnCO_3$ (99.8% purity), were mixed according to their stoichiometric formula and ball milled for 12 h in a nylon jar with zirconia balls as the medium. The dried slurries were calcined for 3 h at 960 °C. The calcined powders were uniaxially pressed into pellets 10 mm in diameter, and the green bodies covered with alumina crucibles were sintered at 1020–1050 °C for 4 h.

Before the electrical measurements, gold films (not silver paste) were chosen to be sputtered on the surfaces of the ceramic pellets to prevent the silver paste electrodes from affecting the state of the defect dipoles during the high-temperature treatment. The dielectric spectra of the samples were measured via an Alpha-A high-performance frequency analyzer (Model CP80, Holocentric Technologies, Germany). The ferroelectric hysteresis loops, bipolar strain curves, and current-electric field curves were measured in silicone oil via a piezoelectric evaluation system (aixPES-TF Analyzer 2000E, aixACCT Systems GmbH, Germany), and the thickness of each sample was fixed at ~0.8 mm before testing.

The crystal structures were characterized via an X-ray diffractometer (XRD; SmartLab9KW, Rigaku, Japan) with Cu Kα radiation. For the *in situ* XRD tests under electric fields, the as-sintered ceramic pellets were sputtered with gold films with an appropriate thickness to prevent X-rays from being absorbed by the electrodes. A field emission scanning electron microscope (FESEM; Merlin, ZEISS, Germany) was carried out to examine the surfaces of the as-sintered ceramic pellets. The microstructures and phases were further analyzed in detail via electron diffraction via a transmission electron microscope (TEM-2100 Plus electron microscope, JEOL, Japan). TSDC characterization was performed with an electrometer/high resistance meter (Keithley 6517B, Keithley Instruments, Inc., USA) via the following procedure. First, the samples were polarized under a DC electric field at a set polarizing temperature and then rapidly cooled to a sufficiently low temperature to freeze the polarization of the defects before field removal. The samples were next heated at a constant heating rate, during which the thermally stimulated depolarization manifested by a depolarization current flowing through the external circuit between electrodes provided the TSDC signal.

3 Results and discussion

3.1 Structures and dielectric properties

The microstructures of the surfaces of the KMN-x ceramics are shown in Fig. 1. This reveals that the addition of a small amount of Mn could cause abnormal growth of the grains. The grain size distributions were assessed via the linear interception method, as shown as insets in Fig. 1. The results show that the grain size increases from 0.527 to 3.808 μm as x increases from 0 to 1.5. Hence, with increasing the Mn content, the average grain size of the ceramics clearly increases, and the grains gradually become homogeneous, which enables the KMN-x ceramics to maintain relatively high densification and therefore to possess good dielectric properties.

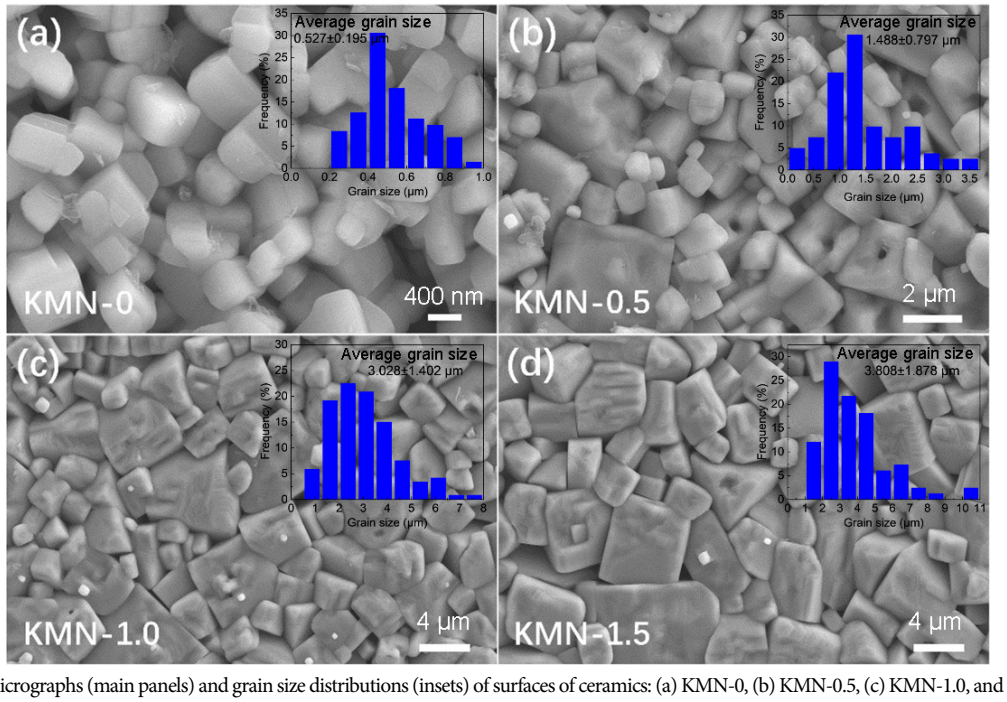

Fig. 1 SEM micrographs (main panels) and grain size distributions (insets) of surfaces of ceramics: (a) KMN-0, (b) KMN-0.5, (c) KMN-1.0, and (d) KMN-1.5.

Figure 2(a) shows the X-ray diffraction patterns of the KMN-x ceramics at room temperature in the range (2θ) of 20°–60°. All the samples possess a single perovskite structure with an orthorhombic phase according to the typical diffraction patterns. To further identify the phase structures in detail, the XRD peaks at approximately 2θ (~45°) are displayed on the right of Fig. 2(a). Compared with that of the KMN-0 sample, the (220) peak of KMN-0.5 moved to a lower angle, indicating that the interplanar distance increased. It is likely that the Mn^{2+} ions (0.67 Å) are dissolved in the matrix of the $KNbO_3$ ceramics without changing the crystal structures of the samples and consequently enter the B-sites of the Nb^{5+} ions (0.64 Å) [45]. However, with further increases in the Mn content, the interplanar distance decreases. It is likely that some of the Mn^{2+} ions are changed into Mn^{3+} ions (0.58 Å) and Mn^{4+} ions (0.53 Å), whose ionic radii are smaller than those of Nb^{5+} ions [45].

The temperature dependence of the dielectric constant (ε_r) and dielectric loss (tanδ) for KMN-x (x = 0–1.5%) at 1 kHz was measured, as shown in Fig. 2(b). Two anomaly peaks can be clearly observed from the KMN-x ceramics. One peak at approximately 250 °C indicates the orthorhombic-tetragonal phase transition. Another peak at approximately 430 °C corresponds to the temperature at which the tetragonal phase transforms into the cubic structure. Compared with that of the KMN-0 sample, T_c of KMN-0.5 slightly decreases at approximately 10 °C, which demonstrates that the addition of $MnCO_3$ has a relatively mild effect on T_c. With increasing Mn content, T_c increases instead. This is probably related to the variation in the valence state of Mn, as the trend of T_c with respect to the Mn content is very similar to that of the diffraction peak at 45° in the XRD patterns. Moreover, the permittivity at room temperature decreases with increasing Mn content. This result also demonstrated that Nb^{5+} was replaced by Mn ions, resulting in a decrease in the intensity of spontaneous polarization.

3.2 Ferroelectric properties and temperature-dependent strain

To further explore the effects of the Mn dopants on the electrical properties of the KMN-x ceramics, the hysteresis loops and bipolar strain curves were tested, and the results are shown in Fig. 3. As a typical ferroelectric phase, excessive oxygen vacancy defects seem to be induced in the KMN-0 sample without Mn doping because of the volatilization of K during high-temperature sintering. Therefore, it shows leakage conduction behavior in a hysteresis loop and an asymmetric butterfly curve of strain, as shown in Fig. 3(a). With the Mn dopants, the KMN-0.5, KMN-1.0, and KMN-1.5 samples show double electric hysteresis loops, and leakage conduction is suppressed (Fig. 3(b)). This is probably related to the formation of defect dipoles such as $Mn_{Nb}^{x} - V_{O}^{\cdot\cdot}$, with interactions between acceptor-doped defects Mn_{Nb}^{x} and excessive oxygen vacancies [46]. This would consequently weaken the irreversibility of non-180° domains. *In situ* XRD under an electric field was used to analyze the contribution of the additional strain of the KMN-0.5 sample shown in Fig. 3(c). The right side of Fig. 3(c) shows the ratio of $I_{(220)}/I_{(002)}$ (the intensity ratio between the (220) peak and the (002) peak in the XRD characterizations) under the applied electric field. The initial ratio of $I_{(220)}/I_{(002)}$ is only 1.8 and gradually increases when the electric field increases, indicating that an increasing number of (002) planes are transformed into (220) planes in the direction parallel to the external electric field. The (110) direction is the spontaneous polarization direction of orthorhombic potassium niobates, which indicates that the non-180° domains switch under an electric field. When the electric field is increased to 4 kV/mm, a peak value of ~4 for the $I_{(220)}/I_{(002)}$ ratio can be achieved, corresponding to a sudden increase in strain (Fig. 3(b)). When the electric field is removed, the value of the $I_{(220)}/I_{(002)}$ ratio decreases to approximately 2.3, which indicates that the non-180° domains switch under an external electric field, whereas the rearranged/reoriented non-180° domains cannot be stable in the absence of an external electric field and can be replaced by switching back.

Combined with the hysteresis loops and bipolar strain curves, the increase in strain in the Mn-doped samples can be attributed to the reversible switching of non-180° domains. When the domains are oriented in the direction of the electric field, the defect dipoles cannot be switched accordingly. Thus, when the electric field is removed, a restoring force could be induced by the difference between the internal electric field caused by defect dipoles and the polarization direction of the domains, as shown in the double electric hysteresis loops. However, with increasing Mn dopant, the existence of defect dipoles has a stronger blocking effect on the polarization of the domains. The maximum polarization and maximum strain of KMN-1.0 and KMN-1.5 decrease under the same electric field.

The electrical properties of the samples at various temperatures were determined. Figures 4(a)–4(c) show the hysteresis loops of KMN-0.5, KMN-1.0, and KMN-1.5, and Figs. 4(d)–4(f) show the bipolar strain curves of KMN-0.5, KMN-1.0, and KMN-1.5 rising from room temperature (25 °C), respectively. The hysteresis loop of KMN-0.5 remains unchanged below 130 °C, but its strain curve begins to decrease when the temperature reaches 100 °C. At the

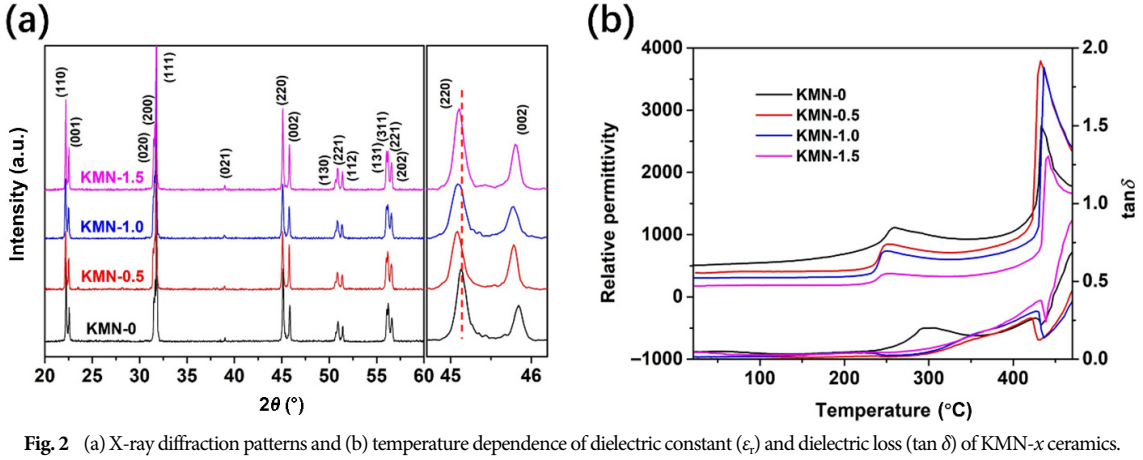

Fig. 2 (a) X-ray diffraction patterns and (b) temperature dependence of dielectric constant (ε_r) and dielectric loss (tan δ) of KMN-x ceramics.

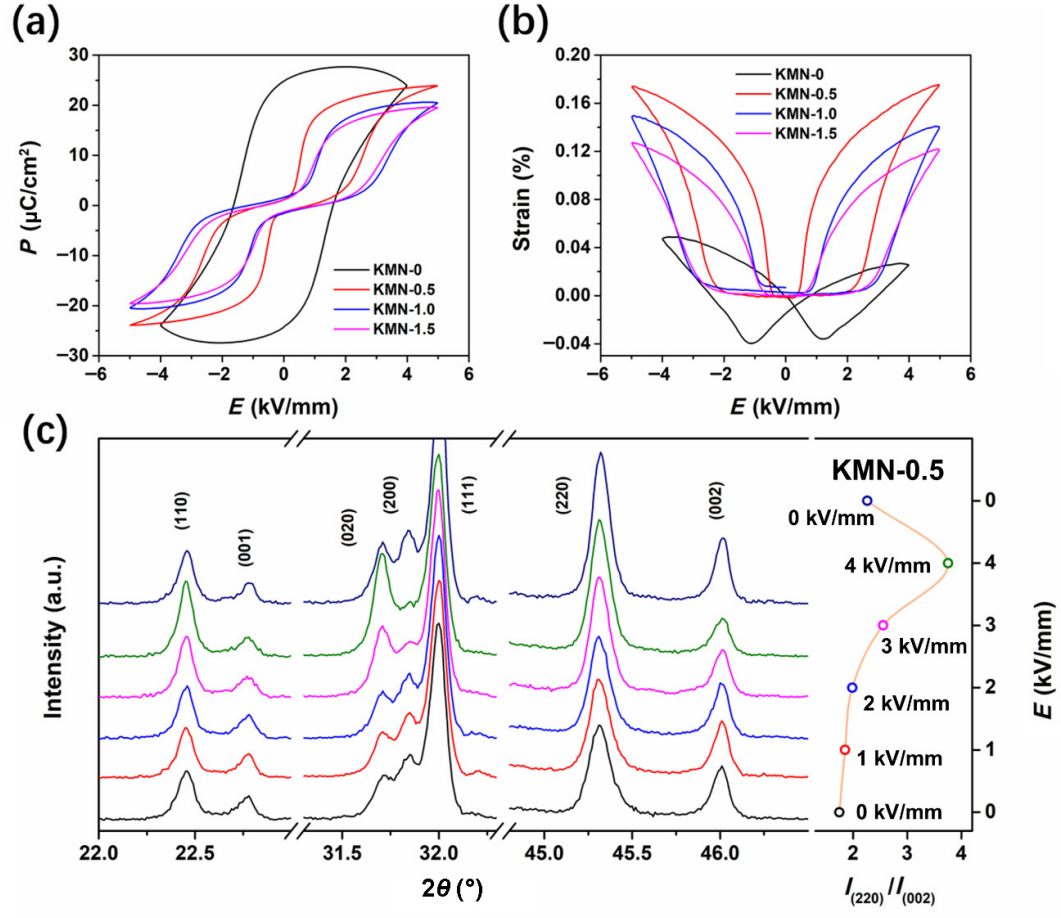

Fig. 3 (a) *P*–*E* hysteresis loops and (b) bipolar strain curves of KMN-*x* ceramics. (c) *In situ* XRD under DC electric field of KMN-0.5 sample.

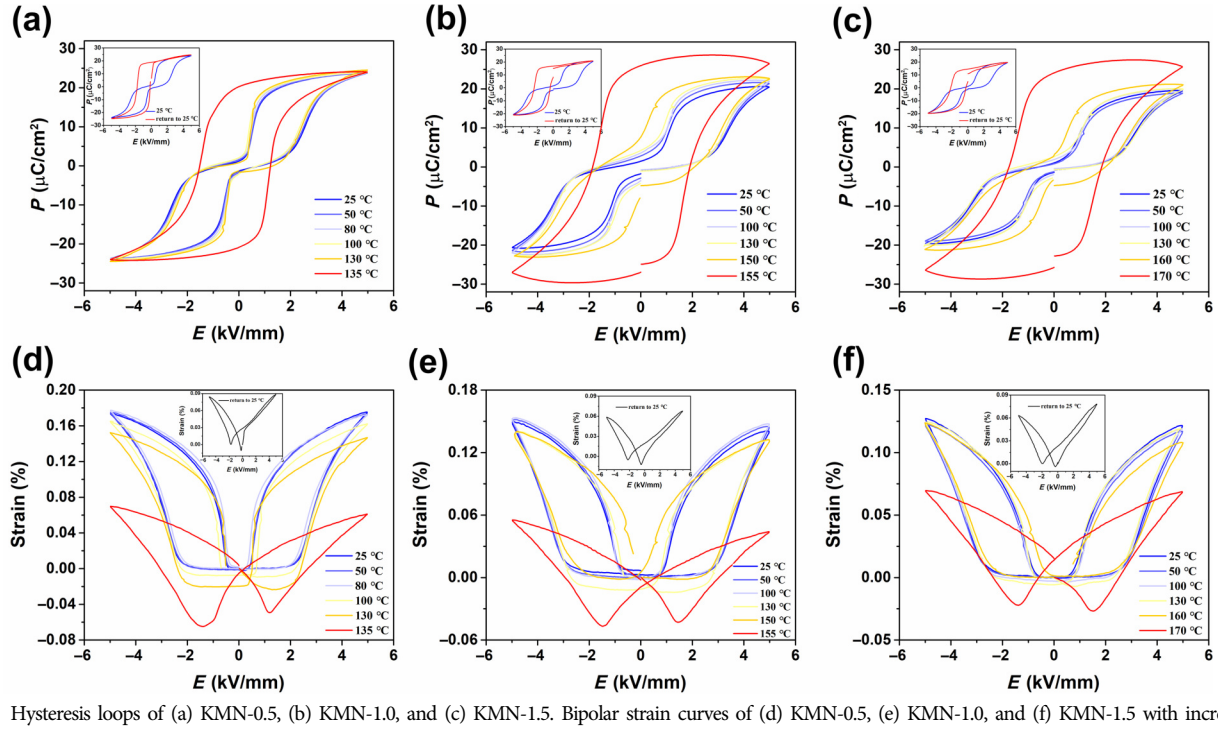

Fig. 4 Hysteresis loops of (a) KMN-0.5, (b) KMN-1.0, and (c) KMN-1.5. Bipolar strain curves of (d) KMN-0.5, (e) KMN-1.0, and (f) KMN-1.5 with increasing temperatures from 25 to 170 °C where the insets are hysteresis loops and bipolar strain curves of KMN-*x* cooled to 25 °C.

critical temperature of 135 °C, the double electric hysteresis loop disappears and becomes a conventional ferroelectric hysteresis loop, and the strain curve becomes a butterfly curve. When the temperature is reduced to 25 °C, the hysteresis loop clearly shows bias. The coercivity field is on the same side of the *y*-axis (the inset of Fig. 4(a)), and the strain curve has a similar bias phenomenon

(the inset of Fig. 4(d)). The results show that the defect dipoles $Mn_{Nb}^{x} - V_{O}^{\cdot\cdot}$ can maintain a stable structure below the critical temperature. Above the critical temperature, under the driving force of thermal activation and an electric field, the original state of the defect dipoles becomes unstable and rearranged. The internal electric field caused by defect dipoles is no longer isotropic on the basis of the symmetry of the electric field, and the strain also decreases significantly to ~0.07%, which is similar to that of KMN-0.

The KMN-1.0 and KMN-1.5 samples with greater Mn contents also have similar trends. With increasing Mn content, the critical temperature of irreversible change also increases significantly, that is, 155 °C for KMN-1.0 and 170 °C for KMN-1.5. In addition, it is worth noting that there is no obvious reduction in the strain below the critical temperature, which indicates that the strain stability under high temperatures can be improved by increasing the content of defect dipoles.

Figures 5(a)–5(c) show the hysteresis loops of the KMN-0.5, KMN-1.0, and KMN-1.5 samples cooled from room temperature (25 °C). Owing to the limitations of test conditions, the strain at low temperatures cannot be measured. Therefore, the electrical properties at low temperatures are analyzed by combining the corresponding electric field and current curves (Figs. 5(d)–5(f)). At 25 °C, the current curve of KMN-0.5 has two pairs of double peaks (Fig. 5(d)), which correspond to the polarization orientation of the domains under an electric field and the recovery of the domains in the process of removing the electric field. When the temperature gradually decreases, the polarization intensity of the hysteresis loop of KMN-0.5 increases, but it still maintains a pinched hysteresis loop. Moreover, the current peak in the current–voltage curve remains unchanged. The reversible switching of non-180° electric domains is the major contributor to the strain, so it can be inferred that the strain of KMN-0.5 also remains stable. When the temperature decreases to −90 °C, the pinched phenomenon of the hysteresis loop clearly disappears, accompanied by sudden splitting of the current peak. This is related to the change in the spontaneous polarization direction caused by the orthorhombic–to–rhombohedral phase transition in potassium niobates. The direction of the defect dipoles acting on the polarized domain changes, and the strain may change accordingly. However, it should be noted that failure at low temperatures is not irreversible, similar to that at high temperatures. When the temperature returns to room temperature, the hysteresis loop and the electric field current curve almost coincide with the state before cooling, which indicates that the structure of the defect dipoles seems stable when only the electric field is applied at low temperature. Therefore, when the temperature increased to room temperature, KMN-0.5 returned to the original orthorhombic phase. The defect dipoles can still be switched back to the polarized domain and maintain the same hysteresis loop as the state before cooling. KMN-1.0 and KMN-1.5 share similar trends, but their critical temperatures show some differences. Specifically, as the Mn content increases from 1.0% to 1.5%, the critical temperature at low temperatures increases from −70 to −60 °C. In conclusion, the stable ranges of the hysteresis loops of KMN-0.5, KMN-1.0, and KMN-1.5 are −80–130, −65–150, and −55–160 °C, respectively. According to the above analysis, our reported electrostrain (0.17% of KMN-0.5) is higher than that reported for piezoelectric ceramics [46,47], and the temperature range (−55–160 °C in KMN-1.5) is wider than that reported for $Na_{0.5}K_{0.5}NbO_3$-based ceramics (25–158 °C) [46].

3.3 Analysis of structural changes at high temperatures

To analyze the structural changes in the KMN-*x* samples with reduced strain properties at high temperatures, TSDC was used to investigate the defect behavior of the ceramics, especially for the defect dipoles. The results are shown in Fig. 6. Two peaks can be observed in each curve (Fig. 6(a)). The sharp current peak at approximately 200 °C is caused by the transition of KMN from the orthorhombic phase to the tetragonal phase. With increasing the Mn content, the phase transition temperature decreases slightly, which is consistent with the temperature dependence of

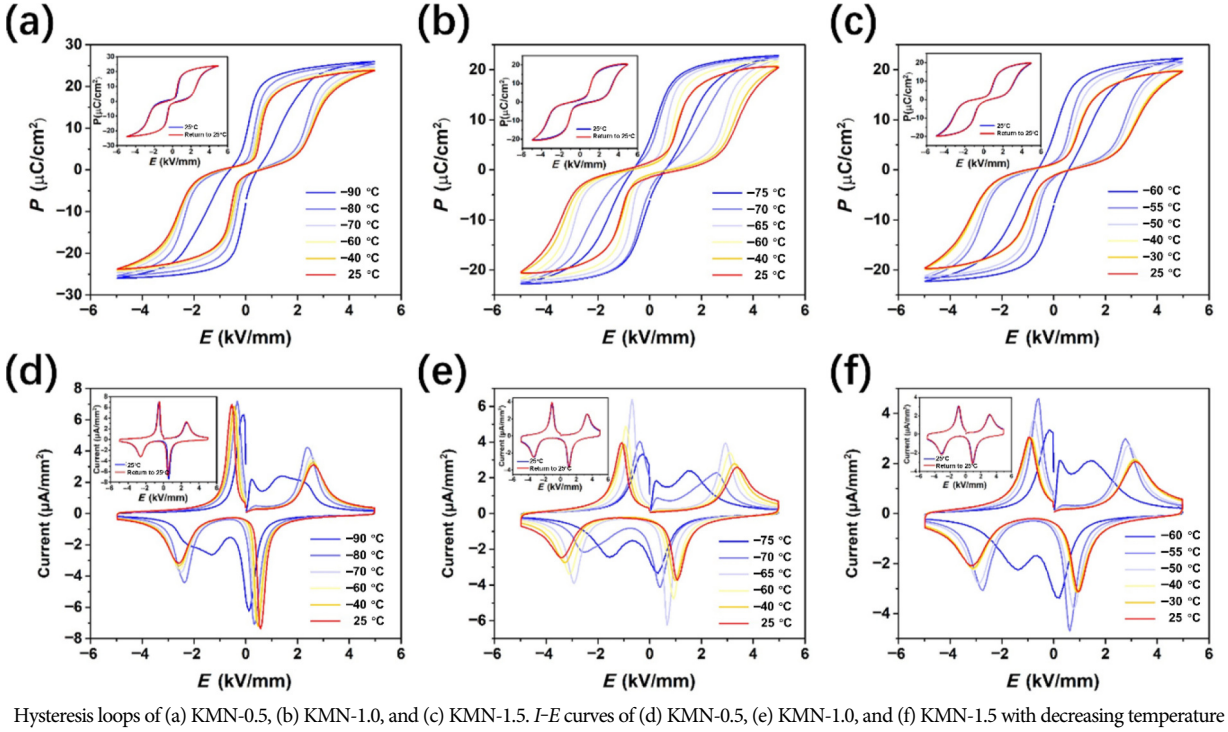

Fig. 5 Hysteresis loops of (a) KMN-0.5, (b) KMN-1.0, and (c) KMN-1.5. *I*–*E* curves of (d) KMN-0.5, (e) KMN-1.0, and (f) KMN-1.5 with decreasing temperature from 25 to −90 °C where the insets are the hysteresis loops and *I*–*E* curves of KMN-*x* cooled to 25 °C.

the dielectric constant [48]. Moreover, a wider TSDC peak occurs at approximately 140 °C. To further elucidate the origin of such defect behavior, the TSDC curves of the KMN-1.5 sample against different polarization electric fields with a fixed polarization temperature are shown in Fig. 6(b). T_m (the temperature where the maximum peak value of the TSDC relaxations occurs) values of the TSDC relaxations clearly remain almost unchanged as the polarization electric field increases. This shows the typical relaxation of defect dipoles, which are more likely to form a defect complex $Mn_{Nb}^{x} - V_{O}^{\cdot\cdot}$, with the interactions of acceptor-doped defects and oxygen vacancies. When the Mn content increases, the current peak moves slightly to high temperatures, which is consistent with the strain stability at high temperatures (Fig. 4). Moreover, the current peak value of the Mn-doped samples is significantly lower than that of the undoped KMN, which indicates that some oxygen vacancies could be trapped by the formation of $Mn_{Nb}^{x} - V_{O}^{\cdot\cdot}$ defect dipoles [42].

The TSDC results for different Mn contents at different polarization temperatures are shown in Fig. 7, and the insets show the details of enlarged images below 200 °C. For the TSDC peaks of each KMN-x ceramic (x = 0, 0.5, 1.0, and 1.5) above 250 °C, the T_m and peak values almost always increase with increasing polarization (in terms of the limitation of the test temperature range), which is closely related to the relaxation of oxygen vacancies. Therefore, oxygen vacancies and defect dipoles were considered the main types of defects present in the title ceramics. When the polarization temperature increases, the current peak corresponding to the defect dipoles increases and then moves to a

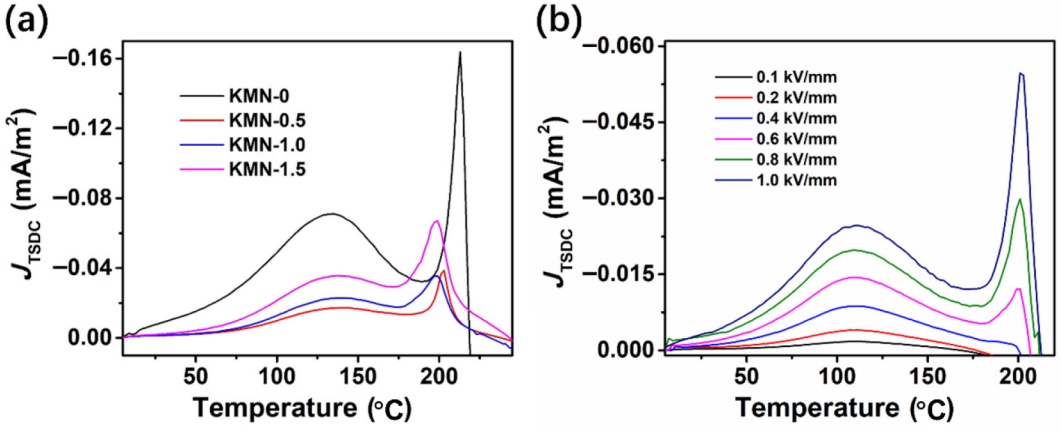

Fig. 6 (a) TSDC results of KMN-x (x = 0, 0.5, 1.0 and 1.5) with polarization temperature of 125 °C where J_{TSDC} refers to the recorded depolarization current density. (b) TSDC results of KMN-1.5 with different electric fields and polarization temperatures of 100 °C.

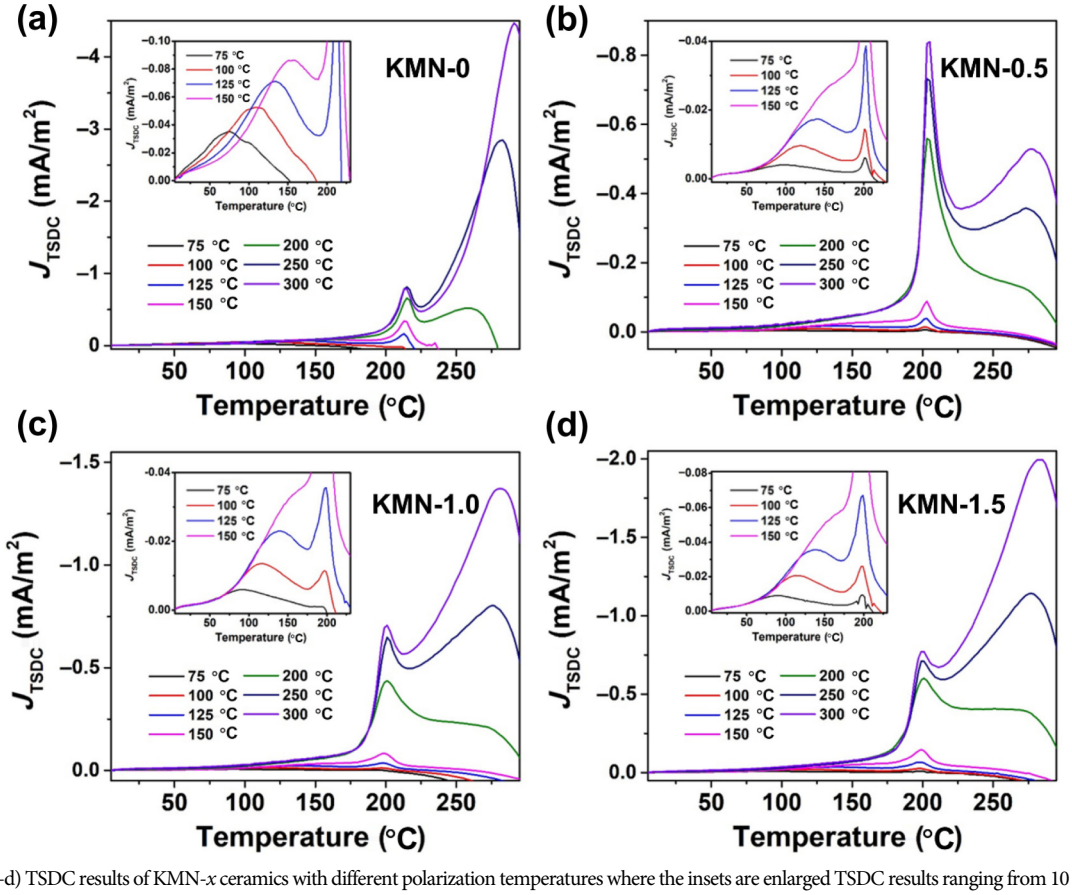

Fig. 7 (a–d) TSDC results of KMN-x ceramics with different polarization temperatures where the insets are enlarged TSDC results ranging from 10 to 230 °C.

high temperature, which indicates that the oxygen vacancy defects associated with $Mn_{Nb}^{x} - V_{O}^{\cdot\cdot}$ are gradually thermally activated. Considering the variation in strain properties, it can be inferred that the thermally activated oxygen vacancies migrate and directionally gather under the electric field, and the defect dipoles become unstable and reorient.

A comparison of the TEM results for the polarized KMN-0.5 and KMN-0.5 samples at high temperatures is shown in Fig. 8. The domain morphology of the polarized KMN-0.5 samples is displayed in Figs. 8(a), 8(e), and 8(f). The distribution area of the domains in the grains is larger than that of the sample that experienced high temperature (Figs. 8(d) and 8(g)), which is related to the pulling back of the polarized domains by the defect dipoles and the pinched hysteresis loops. In addition, different regions of the same grains of the polarized KMN-0.5 sample show different selected area electron diffraction (SAED) patterns under the [1$\bar{1}$0] zone axis. The ½{110} superdiffraction spots appear in the zone III region (Fig. 8(c)), neither zone I nor zone II (Fig. 8(b)). The appearance of the superdiffraction spots may be related to the local distortion of the oxygen octahedra. However, no similar superdiffraction spots can be detected in the samples subjected to high temperatures, which may be related to the rearrangement of oxygen vacancies.

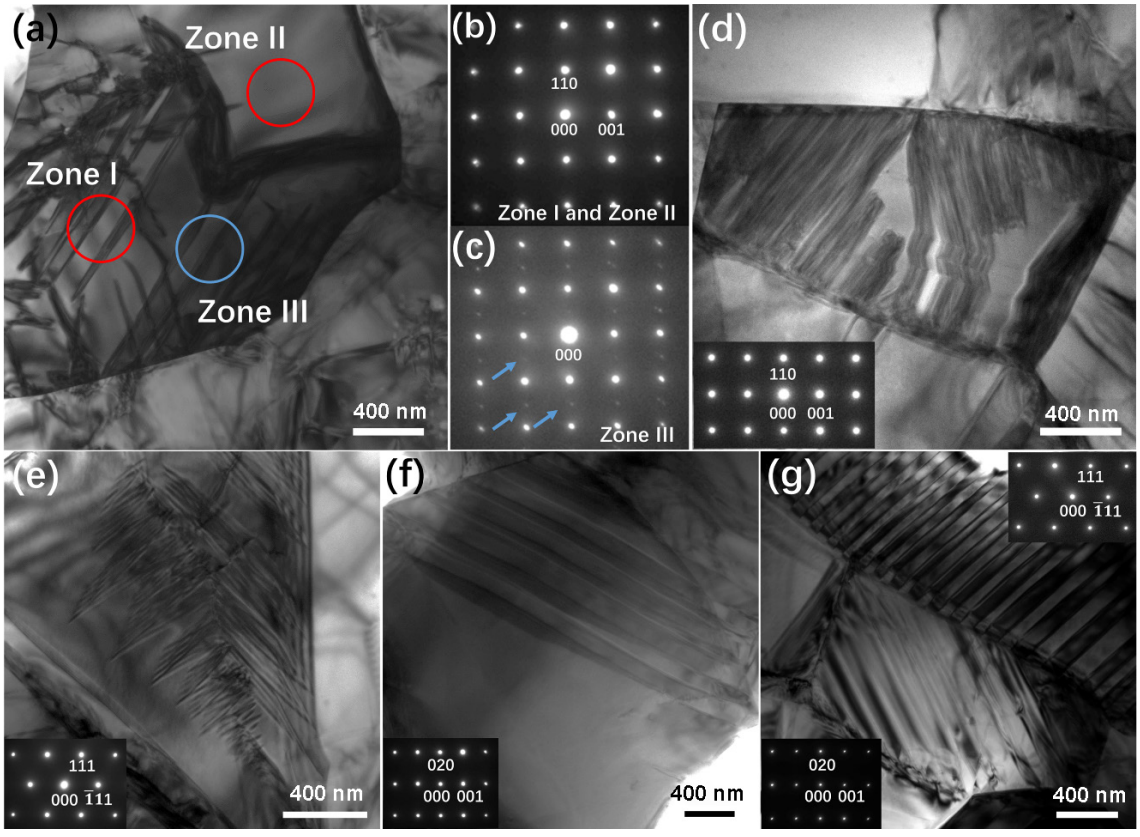

Fig. 8 (a, e, f) TEM images of polarized KMN-0.5; (d) samples experienced high temperatures; (g) ferroelectric domains. Selected area electron diffraction (SAED) patterns along [1$\bar{1}$0] zone axis of zone I, (b)zone II, and (c) zone III.

To further understand the mechanisms of strain reduction caused by structural changes at high temperatures, a corresponding schematic is depicted in Fig. 9. In the initial state, the symmetry of the defect dipoles tends to follow the crystal symmetry of the matrix, and the direction of the internal electric field is consistent with the spontaneous polarization of the surrounding crystals. The defect dipoles are randomly distributed in the grains, so the effects of the internal electric field become isotropic. When an external electric field is applied, the polarization direction of the domains switches along the direction of the electric field, whereas the direction of the internal electric field remains unchanged. Therefore, the chaotic internal electric field pulls the unstable domains back to the initial state without external electric field maintenance, so reversible strain is realized and residual polarization is reduced. At high temperatures, the thermally activated oxygen vacancies migrate to the grain boundaries under the enhanced driving force of the external electric field, and the defect dipoles become unstable. When the temperature decreases back to room temperature, the internal

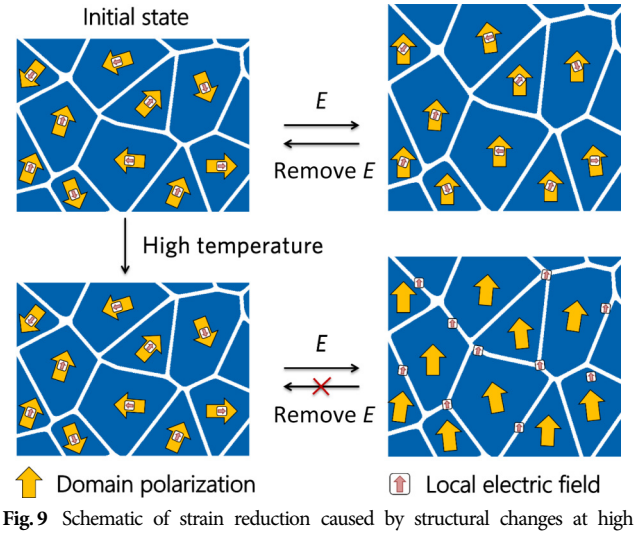

Fig. 9 Schematic of strain reduction caused by structural changes at high temperatures.

清華大学出版社 Tsinghua University Press | SciOpen

electric field also moves to the grain boundary with the restabilization of the oxygen vacancies, inducing a directional electric field. It can counteract the external electric field in a certain direction. As a result, the hysteresis loops show an obvious bias phenomenon, and the fundamental reason is the transition from isotropy to anisotropy of the internal electric field.

4 Conclusions

In conclusion, reversible switching of non-180° domains can be realized by introducing point defects, and the electrostrain can be increased significantly. In this work, recoverable failure at low temperatures and irreversible failure at high temperatures were confirmed by studying the strain properties and stability of defects at different temperatures. Combined with the results of the TSDC analysis, the failure mechanisms for electrostrain in a high-temperature environment were associated with the synergistic damage of the electric field and high temperature on defects. Therefore, improving the high-temperature stability of oxygen vacancies is key for realizing actuator applications at high temperatures. Moreover, this study provides an effective method for understanding the behavior of oxygen vacancy defects in ferroelectric materials.

Acknowledgements

This research was supported by the National Natural Science Foundation of China (Grant Nos. 12135019 and 52202154), the 2115 Talent Development Program of China Agricultural University, the Scientific Research Start-up Fund for Outstanding Talent of China Agricultural University, Chinese Universities Scientific Fund, and High-performance Computing Platform of China Agricultural University.

Declaration of competing interest

The authors have no competing interests to declare that are relevant to the content of this article.

References

[1] Zhang MH, Hu CP, Zhou Z, *et al.* Determination of polarization states in (K,Na)NbO_3 lead-free piezoelectric crystal. *J Adv Ceram* 2020, **9**: 204–209.
[2] Huangfu G, Zeng K, Wang BQ, *et al.* Giant electric field-induced strain in lead-free piezoceramics. *Science* 2022, **378**: 1125–1130.
[3] Rödel J, Jo W, Seifert KTP, *et al.* Perspective on the development of lead-free piezoceramics. *J Am Ceram Soc* 2009, **92**: 1153–1177.
[4] Panda PK, Sahoo B. PZT to lead free piezo ceramics: A review. *Ferroelectrics* 2015, **474**: 128–143.
[5] Hu CP, Meng XD, Zhang MH, *et al.* Ultra-large electric field-induced strain in potassium sodium niobate crystals. *Sci Adv* 2020, **6**: eaay5979.
[6] Zhao PY, Li LT, Wang XH. $BaTiO_3$–$NaNbO_3$ energy storage ceramics with an ultrafast charge–discharge rate and temperature-stable power density. *Microstructures* 2022, **3**: 2022023.
[7] Takenaka T, Nagata H. Current status and prospects of lead-free piezoelectric ceramics. *J Eur Ceram Soc* 2005, **25**: 2693–2700.
[8] Liu Z, Lu T, Xue F, *et al.* Lead-free (Ag,K)NbO_3 materials for high-performance explosive energy conversion. *Sci Adv* 2020, **6**: eaba0367.
[9] Gao XY, Cheng ZX, Chen ZB, *et al.* The mechanism for the enhanced piezoelectricity in multi-elements doped (K,Na)NbO_3 ceramics. *Nat Commun* 2021, **12**: 881.
[10] Wu JG. Perovskite lead-free piezoelectric ceramics. *J Appl Phys* 2020, **127**: 190901.
[11] Wu XJ, Wen LJ, Wu C, *et al.* Insight into the large electro-strain in bismuth sodium titanate-based relaxor ferroelectrics: From fundamentals to regulation methods. *J Mater Sci Technol* 2023, **150**: 27–48.
[12] Wang XP, Wu JG, Xiao DQ, *et al.* Giant piezoelectricity in potassium–sodium niobate lead-free ceramics. *J Am Chem Soc* 2014, **136**: 2905–2910.
[13] Liu XM, Tan XL. Giant strains in non-textured ($Bi_{1/2}Na_{1/2}$)TiO_3-based lead-free ceramics. *Adv Mater* 2016, **28**: 574–578.
[14] Choi SY, Jeong SJ, Lee DS, *et al.* Gigantic electrostrain in duplex structured alkaline niobates. *Chem Mater* 2012, **24**: 3363–3369.
[15] Wang K, Li JF. (K,Na)NbO_3-based lead-free piezoceramics: Phase transition, sintering and property enhancement. *J Adv Ceram* 2012, **1**: 24–37.
[16] Li CBW, Li Z, Wang J, *et al.* Sodium lithium niobate lead-free piezoceramics for high-power applications: Fundamental, progress, and perspective. *J Adv Ceram* 2023, **12**: 1–23.
[17] Xu K, Li J, Lv X, *et al.* Superior piezoelectric properties in potassium–sodium niobate lead-free ceramics. *Adv Mater* 2016, **28**: 8519–8523.
[18] Wang J, Wang BQ, Zhang HJ, *et al.* Ultrahigh electrobending deformation in lead-free piezoelectric ceramics via defect concentration gradient design. *Adv Mater* 2024, **36**: e2404682.
[19] Hu ZM, Koval V, Zhang HF, *et al.* Enhanced piezoelectricity in Na and Ce co-doped $CaBi_4Ti_4O_{15}$ ceramics for high-temperature applications. *J Adv Ceram* 2023, **12**: 1331–1344.
[20] Yao FZ, Wang K, Jo W, *et al.* Diffused phase transition boosts thermal stability of high-performance lead-free piezoelectrics. *Adv Funct Mater* 2016, **26**: 1217–1224.
[21] Zhang MH, Wang K, Du YJ, *et al.* High and temperature-insensitive piezoelectric strain in alkali niobate lead-free perovskite. *J Am Chem Soc* 2017, **139**: 3889–3895.
[22] Wang XJ, Wang J, Geng WP, *et al.* Large electrical strain in lead-free $K_{0.5}Na_{0.5}NbO_3$-based ceramics by heterovalent doping. *J Materiomics* 2023, **9**: 959–970.
[23] Yan YK, Zhou JE, Maurya D, *et al.* Giant piezoelectric voltage coefficient in grain-oriented modified $PbTiO_3$ material. *Nat Commun* 2016, **7**: 13089.
[24] Jiang LM, Tan Z, Xie LX, *et al.* Study of the relationships among the crystal structure, phase transition behavior and macroscopic properties of modified (K,Na)NbO_3-based lead-free piezoceramics. *J Eur Ceram Soc* 2018, **38**: 2335–2343.
[25] Wang X, Sun XX, Yang YX, *et al.* Modified re-entrant-like (K,Na)NbO_3-based relaxors with superior electrostrain properties. *Adv Funct Mater* 2024: 2406154.
[26] Tian A, Yu ZD, Xie AW, *et al.* Multiple local polarization configurations in NKN-based relaxor ferroelectric ceramic with high electrostrictive-like strain. *J Eur Ceram Soc* 2024, **44**: 7614–7622.
[27] Feng ZY, Ren XB. Aging effect and large recoverable electrostrain in Mn-doped $KNbO_3$-based ferroelectrics. *Appl Phys Lett* 2007, **91**: 032904.
[28] Feng ZY, Or SW. Aging-induced, defect-mediated double ferroelectric hysteresis loops and large recoverable electrostrains in Mn-doped orthorhombic $KNbO_3$-based ceramics. *J Alloys Compd* 2009, **480**: L29–L32.
[29] Kim JH, Kim DH, Lee TH, *et al.* Large electrostrain in K($Nb_{1-x}Mn_x$)O_3 lead-free piezoelectric ceramics. *J Am Ceram Soc* 2016, **99**: 4031–4038.
[30] Tian A, Zuo RZ, Qi H, *et al.* Large energy-storage density in transition-metal oxide modified $NaNbO_3$–Bi($Mg_{0.5}Ti_{0.5}$)O_3 lead-free ceramics through regulating the antiferroelectric phase structure. *J Mater Chem A* 2020, **8**: 8352–8359.
[31] Feng ZY, Ren XB. Striking similarity of ferroelectric aging effect in tetragonal, orthorhombic and rhombohedral crystal structures. *Phys Rev B* 2008, **77**: 134115.
[32] Luo NN, Ma L, Luo GG, *et al.* Well-defined double hysteresis loop in $NaNbO_3$ antiferroelectrics. *Nat Commun* 2023, **14**: 1776.
[33] Luo HJ, Liu H, Huang HB, *et al.* Achieving giant electrostrain of above 1% in (Bi,Na)TiO_3-based lead-free piezoelectrics via introducing oxygen-defect composition. *Sci Adv* 2023, **9**: eade7078.

[34] Wang BQ, Huangfu G, Wang J, *et al.* Defect dipole-induced fatigue strain recoverability in lead-free piezoelectric ceramics. *Adv Funct Mater* 2023, **33**: 2306416.
[35] Lai LX, Li B, Tian S, *et al.* Giant electrostrain in lead-free textured piezoceramics by defect dipole design. *Adv Mater* 2023, **35**: e2300519.
[36] Feng W, Luo BC, Bian SS, *et al.* Heterostrain-enabled ultrahigh electrostrain in lead-free piezoelectric. *Nat Commun* 2022, **13**: 5086.
[37] Tian S, Wang BQ, Li B, *et al.* Defect dipole stretching enables ultrahigh electrostrain. *Sci Adv* 2024, **10**: eadn2829.
[38] Cen ZY, Feng MY, Cao FZ, *et al.* Improving high-field strain and temperature stability on KNN-based ceramics sintered in reducing atmosphere via defect engineering. *J Materiomics* 2024, **10**: 1165–1175.
[39] Ma HS, Lee MK, Kim BH, *et al.* Role of oxygen vacancy defects in piezoelectric thermal stability characteristics of Mn-doped (K,Na,Li)NbO_3 piezoceramics. *Ceram Int* 2021, **47**: 27803–27815.
[40] Liu Q, Zhu FY, Zhao L, *et al.* Further enhancing piezoelectric properties by adding MnO_2 in $AgSbO_3$–modified (Li,K,Na)(Nb,Ta)O_3 lead-free piezoceramics. *J Am Ceram Soc* 2016, **99**: 3670–3676.
[41] Mgbemere HE, Hinterstein M, Schneider GA. Structural phase transitions and electrical properties of $(K_xNa_{1-x})NbO_3$-based ceramics modified with Mn. *J Eur Ceram Soc* 2012, **32**: 4341–4352.
[42] Zhang J, Yue ZX, Zhou YY, *et al.* Microwave dielectric properties and thermally stimulated depolarization currents of $(1-x)MgTiO_3$–$xCa_{0.8}Sr_{0.2}TiO_3$ ceramics. *J Am Ceram Soc* 2015, **98**: 1548–1554.
[43] Hao JG, Shen B, Zhai JW, *et al.* Switching of morphotropic phase boundary and large strain response in lead-free ternary $(Bi_{0.5}Na_{0.5})TiO_3$–$(K_{0.5}Bi_{0.5})TiO_3$–$(K_{0.5}Na_{0.5})NbO_3$ system. *J Appl Phys* 2013, **113**: 114106.
[44] Liu W, Randall CA. Thermally stimulated relaxation in Fe-doped $SrTiO_3$ systems: I. *single crystals. J Am Ceram Soc* 2008, **91**: 3245–3250.
[45] Shannon RD. Dielectric polarizabilities of ions in oxides and fluorides. *J Appl Phys* 1993, **73**: 348–366.
[46] Cen ZY, Bian SS, Xu Z, *et al.* Simultaneously improving piezoelectric properties and temperature stability of $Na_{0.5}K_{0.5}NbO_3$ (KNN)-based ceramics sintered in reducing atmosphere. *J Adv Ceram* 2021, **10**: 820–831.
[47] Chen Y, Li LF, Zhou Z, *et al.* La_2O_3-modified $BiYbO_3$–Pb(Zr,Ti)O_3 ternary piezoelectric ceramics with enhanced electrical properties and thermal depolarization temperature. *J Adv Ceram* 2023, **12**: 1593–1611.
[48] Li P, Chen XQ, Wang FF, *et al.* Microscopic insight into electric fatigue resistance and thermally stable piezoelectric properties of (K,Na)NbO_3-based ceramics. *ACS Appl Mater Inter* 2018, **10**: 28772–28779.